RSC Advances

PAPER

View Article Online
View Journal | View Issue

Cite this: *RSC Adv.*, 2025, **15**, 33252

Atomic-scale engineering of Fe–Cu nanoparticles on amine-functionalized silica: CNT-driven synergy for ultra-efficient hydrogen evolution

Nezar H. Khdary, *[a] Ekram H. El-Ads,[b] Ahmed Galal, [b] Ahmad O. Fallatah,[a] Sami D. Alzahrain,[a] Muteb F. Alotaibi[a] and Mohammed J. Alotaibi[a]

Received 26th May 2025
Accepted 8th August 2025

DOI: 10.1039/d5ra03709c

rsc.li/rsc-advances

Emphasizing a breakthrough in material synergy and synthesis strategies, this work provides a new catalyst design for high-efficiency electrolytic water splitting. The novelty is in the development of a hierarchical Fe/Cu@silica-CNT composite, whereby exact anchoring of Fe^{3+}/Cu^{2+} ions is enabled by silica functionalization with *N*-(3-(trimethoxysyl)propyl)ethylenediamine, consequently guaranteeing atomic-level metal distribution and preventing nanoparticle aggregation. A significant improvement over conventional deposition techniques resulted from subsequent chemical reduction, producing ultra-small, stable Fe/Cu nanoparticles (5 nm) directly grafted onto silica. The use of multi-walled carbon nanotubes (CNTs) generated a three-dimensional conductive network, which simultaneously optimized charge transfer and achieved nanoparticle dispersion. Extensive characterization (FE-SEM, EDX, XPS, and BET) confirmed that the high-density active sites at Fe/Cu–SiO_2 interfaces, coupled with CNT-induced electron delocalization, validate the uniqueness of the architecture. Under acidic conditions, electrochemical testing revealed remarkable hydrogen evolution reaction (HER) performance with a record-low Tafel slope of 34 mV dec^{-1} and an overpotential reduction of 120 mV against bare CNTs. Fe–Cu electronic interactions and CNT-mediated mass transport resulted in a 4.3-fold increase in exchange current density that the catalyst achieved relative to its monometallic counterparts. This work presents a transforming solution for scalable green hydrogen generation using a creative dual-engineering approach, molecular-scale metal anchoring, and a nano-architecture conductive support, thus solving major obstacles in catalyst durability and activity.

1. Introduction

The global transition to sustainable energy systems has intensified the search for clean, efficient, and scalable methods for producing hydrogen (H_2), a carbon-neutral energy carrier that has the potential to decarbonize power generation, transportation, and industry. Among the various methods for producing H_2, water splitting, either by electrochemical, photochemical, or thermochemical processes, stands out as a key technology. Water is the most abundant resource on Earth. Advanced catalysts are required to lower the energy barriers and increase the reaction rates of water splitting because the efficiency and cost of water splitting are still constrained by the slow kinetics of the HER and oxygen evolution reaction (OER).[1] Even though noble metals such as platinum are still the gold standard for HER catalysis, their high cost and limited availability have sparked research on earth-abundant alternatives. Copper has emerged as a potential HER catalyzing agent due to its unique electronic properties, affordable price, and versatility in creating active nanostructures. According to recent research, a film of Cu(0)-based nanoparticles that is produced by *in situ* electrochemical reduction of Cu(II) ions on modified silica demonstrates remarkable activity and durability as a catalyst for the HER in acidic solutions.[2] Copper-based materials, including nanoparticles, oxides, and sulfide compounds, are currently being explored as catalysts for high-efficiency electrolysis (HER) technology. These catalysts are effective in both acidic and alkaline environments. This versatility means that the same catalyst material can be used in different types of electrolytic cells, which may operate under varying acidity conditions. Nanostructured Cu_2O/Cu heterojunctions have demonstrated, for example, a low overpotential of 120 mV at 10 mA cm^{-2} and improved charge transfer efficiency in alkaline electrolytes.[3] Moreover, enhancing copper's catalytic conductivity and durability increases its capacity to coordinate with carbon matrices or transition metal dichalcogenides, such as MoS_2.[4,5] These developments have helped copper to become a scalable and controllable material for large-scale hydrogen-producing systems.

Because of its low cost, environmental friendliness, and high theoretical activity, iron, the most plentiful transition metal in Earth's crust, offers unmatched benefits to produce sustainable

[a]*King Abdulaziz City for Science and Technology, Riyadh 11442, Kingdom of Saudi Arabia. E-mail: nhkdary@kacst.edu.sa*

[b]*Cairo University, Faculty of Science, Chemistry Department, Giza, 12613, Egypt*

hydrogen. Under ideal conditions, recent developments in iron-based catalysts, carbides, Fe_3O_4 nanoparticles, and Fe–N–C coordination complexes show remarkable HER performance on a par with noble metals. Fe single-atom catalysts incorporated into nitrogen-doped graphenes achieved an overpotential of 88 mV at 10 mA cm^{-2} under acidic conditions using favorable adsorption energetics of hydrogen intermediates.[6,7] Fe_2O_3 photoanodes increase charge separation in photoelectrochemical systems, enabling solar-driven water splitting and increasing the adaptability of iron. Given that there are still issues reducing iron's sensitivity to oxidative deterioration and dissolution in watery environments, protective coatings or alloying with metals resistant to corrosion is consequently essential.[8–10] Iron integration into hybrid systems such as Fe–Co phosphides or FeNi layered double hydroxides has improved catalytic stability and bifunctionality for general water splitting.[11] Recent findings have shown that hierarchical Fe_3C@C nanostructures, which comprise iron carbide nanoparticles uniformly encapsulated within graphitic carbon shells, demonstrate remarkable electrocatalytic performance with 95% faradaic efficiency for the HER.[12] Iron-based catalysts will most probably become more important as studies on reaching affordable and ecologically friendly hydrogen economies develop.

In this work, the reason for the combined Fe and Cu is that the Fe and Cu's electronic and geometric interactions improve hydrogen adsorption and desorption, modify the d-band structure, and distribute surface charge. Furthermore, these interactions facilitate the formation of Fe/Cu heterojunctions, creating unique interfacial sites that serve as active centers for the HER. Effective means to increase catalyst dispersion and HER performance are Fe/Cu nanoparticles supported on coordinated-amine-silica. The coordinated amine groups function as electronic mediators; the silica support offers nanoparticles a steady anchoring matrix. This system solves major difficulties in HER catalysis, including low conductivity, limited active site exposure, and nanoparticle aggregation. Carbon nanotubes (CNTs) are also essential due to their ability to enhance electrical conductivity, facilitate electron transport, and enable rapid charge transfer during the HER. Combining Fe/Cu nanoparticles with CNTs and amine-functionalized silica generates a hierarchical catalyst system with many applications. Fe and Cu combined produce a single hybrid catalyst using their "dual functionality". While Fe drives water dissociation to create a cooperative mechanism increasing the HER activity, Cu helps in hydrogen adsorption. By the deliberate mixing of Cu and Fe inside the coordinated-amine-silica matrix, a very strong and long-lasting catalyst system is generated in tandem with CNTs. Faster charge transfer, reduced overpotentials, and increased hydrogen production rates follow from this hybrid interface developed by this metal combination optimizing the electronic structure.

2. Experimental

2.1 Materials and preparations

All chemicals were used as received, without additional purification. Methanol and toluene were sourced from Prolabo (Europe). Sulfuric acid (98%), potassium hydroxide (99.5%), multi-walled carbon nanotubes, copper sulfate pentahydrate, iron(II) chloride tetrahydrate, and iron(III) chloride hexahydrate were obtained from Sigma-Aldrich (USA). *N*-(3-(Trimethoxysilyl) propyl)ethylenediamine and silica gel were purchased from ACROS Organics (USA).

2.2 Characterization

The spectra of the prepared samples were recorded using an ATR-FT-IR spectrometer (Vertex 70, Bruker, Germany) in the range of 500–4000 cm^{-1} with 64 scans and a resolution of 4 cm^{-1}. Thermogravimetric analysis (TGA) was performed to assess the catalyst's properties and degradation behavior using a STD-Q 600 instrument (USA) in a helium atmosphere at a heating rate of 10 °C min^{-1} from 25 to 800 °C. The BET (Brunauer–Emmett–Teller) surface area and pore volume were measured using an ASAP2020 system with high-purity nitrogen. The structure, morphology, and degree of distribution of nanoparticles were determined using a scanning electron microscope (SEM), JEOL JSM-7800F and Transmission electron microscope (TEM), JEOL JEM-2100F, operating at 200 kV. Point and mapping analyses were performed by energy-dispersive X-ray spectroscopy (EDS) using an Oxford Instruments X-Max detector. The composition of the catalyst and electronic states were analyzed using a JPS-9200 X-ray photoelectron spectrometer, with Al Kα radiation ($h\nu = 1486.6$ eV). Inductively coupled plasma (ICP-OES) measurements were conducted using a "Horiba" model "Ultima-Expert LT" (France).

2.3 Modification

The surface functionalization of silica was achieved using ethylenediamine silane coupling agent *N*-[3-(trimethoxysilyl) propyl]ethylenediamine. The reaction was conducted in a 250 mL round-bottom flask equipped with a condenser. To this, 150 mL of dry toluene was added with 5.0 g of silica, and the mixture was stirred under a nitrogen atmosphere. The temperature gradually increased to 70 °C, where it was maintained. Once stable at 70 °C, 3 mL of the functionalizing agent was slowly added to the reaction. The temperature was then increased to 80 °C, and the reaction was allowed to proceed for 7 hours with continuous stirring. Afterward, the reaction mixture was cooled to room temperature. The modified silica particles were separated by centrifugation, thoroughly rinsed with toluene and methanol, and then dried overnight at 50 °C under vacuum. The amine-functionalized silica was labelled "Amine@silica".

For the incorporation of Fe and Cu ions onto modified silica, 0.5 g of the functionalized silica was transferred to a 10 mL screw-top vial. To this, 4 mL of Fe(III) solution and 4 mL of 1.0 M $Cu(SO_4)\cdot 5H_2O$ solution were added simultaneously. The mixture was shaken for 4 hours. Afterwards, the suspension was centrifuged to remove any unreacted material, and the product was rinsed five times with deionized water. Finally, the modified silica was vacuum-dried at 60 °C before characterization.

2.4 Electrochemical instrumentation and cell setup

Electrochemical measurements including voltammetry and chronoamperometry were conducted using a PGSTAT302N

galvanostat/potentiostat (Metrohm, Switzerland) equipped with a FRA32M module. A three-electrode configuration was employed, where an Ag/AgCl reference electrode (3.0 mol per L KCl; the drift in potential was ±2 mV) was used, a glassy carbon electrode (GC) (diameter: 3.0 mm) served as the working electrode, and a platinum wire (length: 10 cm; diameter: 2.0 mm) acted as the auxiliary electrode. Linear sweep voltammetry (LSV) measurements were recorded within the potential range of −0.2 V to −1.1 V *vs.* the reversible hydrogen electrode (RHE) at a scan rate of 5 mV s^{-1}. Tafel plots were generated at a scan rate of 1 mV s^{-1}. Chronoamperometry experiments were conducted by applying a constant potential corresponding to the onset potential of the HER on the catalyst surface for around 2 hours.

2.5 Electrode preparation

A catalyst ink was prepared by physically mixing 1.0 mg of solid catalyst (Fe(III)@silica, Fe(II)/Cu(II)@silica, or Fe(III)/Cu(II)@silica) with 1.0 mL of DMF. To this mixture, 0.5 mg of carbon nanotubes (CNTs) were added, and the resulting blend was sonicated for one hour to ensure uniform distribution of all components. The glassy carbon (GC) electrode surface was then prepared by mechanical polishing with progressively finer grades of polishing paper. Following this, the electrode was cleaned to remove any grease or adsorbed particles using a combination of solvents and sonication in distilled water. The cleaned electrode was then placed in an oven at 60 °C for 10 minutes to dry. The final amount of catalyst deposited on the surface was 10×10^{-6} g. The influence of both the solid silica catalyst quantity and the type of carbon material was examined to determine the optimal catalyst-to-carbon material ratio.

3. Results and discussion

3.1 Characterization of the synthesized nanoparticles

Fig. 1 shows the schematic representation of the primary steps in the synthesis of iron (Fe) and copper (Cu)-coronated silica nanoparticles. The process commenced with the functionalization of silica particles using a silane coupling agent, which introduced amine groups to the silica surface. In the final stage, iron–copper nanoparticles were immobilized onto these amine-functionalized silica particles, resulting in the formation of a stable solid composite material.

Fig. 2 displays the optical image that highlights the distinct colour changes observed throughout the different stages of synthesis. The image shows the visual differences between amine-functionalized silica particles bound to Fe(III), amine-functionalized silica coupled with Fe(II)/Cu(II), and amine-functionalized silica containing both Fe(III) and Cu(II), reflecting the variations in composition and oxidation states during the process.

3.2 SEM, TEM and EDS

Fig. 3(a–c) show the morphological and structural analyses of the Fe(III)/Cu(II)@silica nanocomposite. The low-magnification SEM image (a) displays a smooth silica surface, while the higher magnification image (b) reveals dispersed Fe and Cu nanoparticles without noticeable agglomeration. The high-resolution TEM image (c) confirms the nanoscale distribution of spherical metal nanoparticles, with an average of 5 nm, indicating successful and uniform incorporation of Fe(III) and Cu(II) into the silica matrix. To examine the chemical composition of the Fe(III)/Cu(II)@silica in greater detail, energy-dispersive X-ray spectroscopy (EDS) was employed (Fig. 4), and the corresponding spectrum is shown in the figure. Elemental mapping, using a colour-coded scheme for silicon (Si), oxygen (O), copper (Cu), and iron (Fe), revealed a homogeneous distribution of these elements throughout the nanocomposite. Quantitative elemental analysis identified the following atomic percentages: iron (0.15%), copper (0.27%), oxygen (75.78%), and silicon (23.79%). These results are consistent with the findings from X-ray photoelectron spectroscopy (XPS), further confirming the successful synthesis of the Fe(III)/Cu(II)@silica nanocomposite. This comprehensive analysis of morphology and elemental composition demonstrates the effectiveness of the synthesis process and highlights the well-defined structure

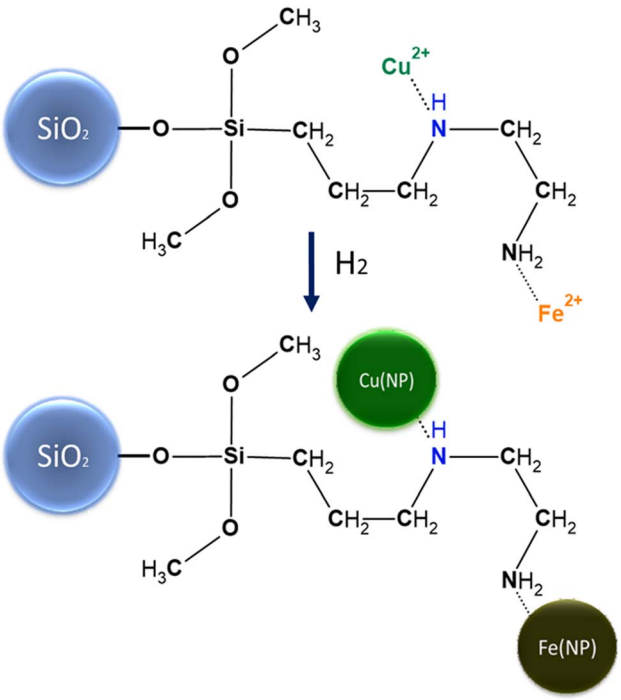

Fig. 1 Schematic of the synthesis route for Fe–Cu nanoparticles on amine-functionalized silica.

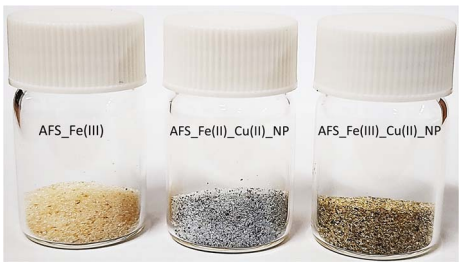

Fig. 2 Optical image showing color variations in amine@silica modified with Fe(III), Fe(II)/Cu(II), and Fe(III)/Cu(II).

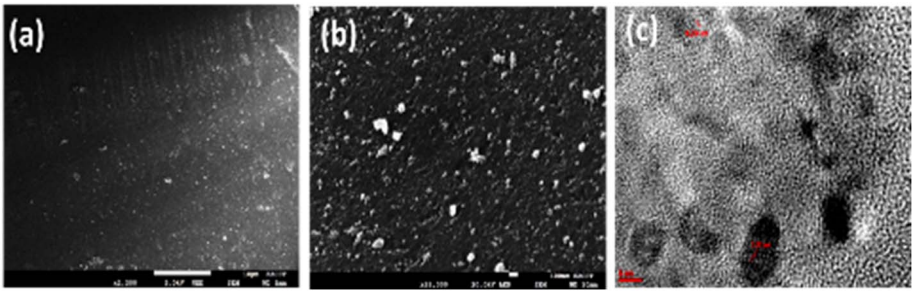

Fig. 3 Scanning electron microscopy (SEM) images of Fe(III)/Cu(II)@silica nanocomposites at low (a) and high (b) magnifications, showing a uniform dispersion of nanoparticles throughout the silica surface without noticeable aggregation. (c) High-resolution transmission electron microscopy (HRTEM) image demonstrating evenly distributed Fe and Cu nanoparticles embedded in the silica matrix.

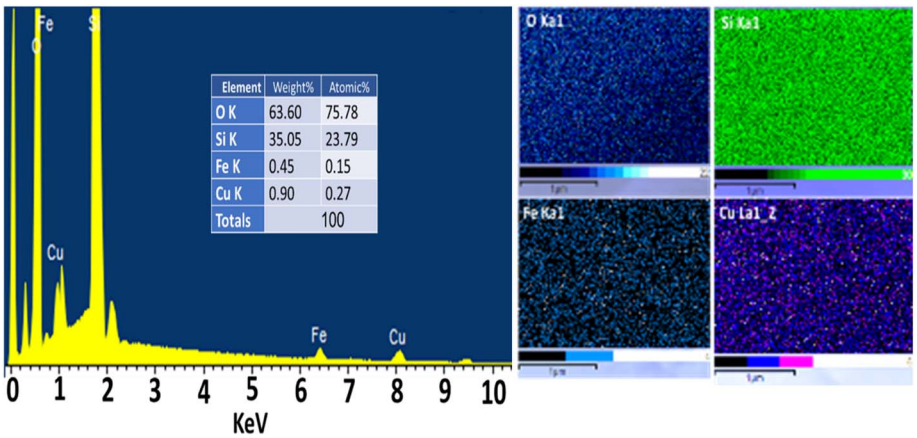

Fig. 4 Energy-dispersive spectroscopy (EDS) analysis and elemental mapping illustrating the distribution of O, Si, Fe, and Cu in Fe(III)/Cu(II)@silica.

and uniform elemental distribution within the nanocomposite, supporting its potential for various scientific and industrial applications.

3.3 FTIR spectra

Fig. 5(a) presents the FTIR spectra of the as-prepared amine@silica, Fe(II)/Cu(II)@silica, and Fe(III)/Cu(II)@silica nanocomposites. A broad absorption band at 3350 cm^{-1} corresponds to the stretching vibrations of O–H and N–H bonds in the amine-based structure and adsorbed water on the nanocomposites. The absorption band observed at 1650 cm^{-1} is associated with the bending vibrations of O–H and N–H bonds, while the peak around 1067 cm^{-1} indicates the vibration mode of S–O bonds in SiO_2 and the silane functional groups[13–16]

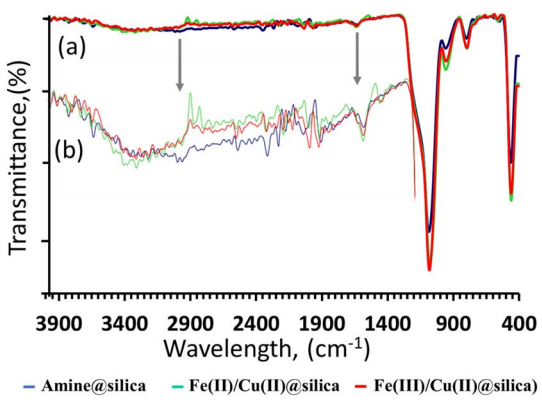

Fig. 5 FTIR spectra comparing amine@silica, Fe(II)/Cu(II)@silica, and Fe(III)/Cu(II)@silica samples: (a) original spectra and (b) enlargement of the three spectra, where blue represents amine@silica, green represents Fe(II)/Cu(II)@silica, and red indicates Fe(III)–Cu(II)@silica.

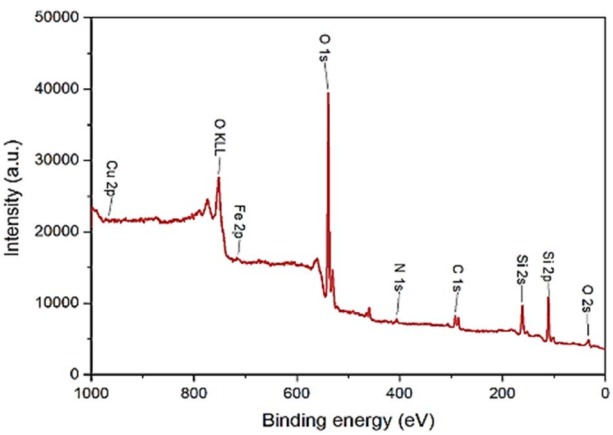

Fig. 6 XPS survey spectrum of Fe(III)/Cu(II)@silica confirming its elemental composition.

Furthermore, the peaks at 956 cm^{-1} and 797 cm^{-1} are attributed to the stretching vibration of C–O–C bonds and the bending vibration of C–H bonds, respectively. The absorption band at 459 cm^{-1} corresponds to the bending vibration of Si–O bonds, and the stretching vibrations of metal–oxygen and metal-nitrogen bonds in the sample's molecular structure.[17–19] Comparing the intensity of this latter peak revealed that the absence of metal cations in the amine@silica sample results in a reduced peak intensity. In contrast, the overlapping of the Fe/Cu–O and Fe/Cu–N bond vibrations with the Si–O bending vibration increases the intensity of the corresponding peak. The spectra are enlarged in Fig. 5(b) for a clearer view.

3.4 X-ray photoelectron spectroscopy (XPS)

X-ray photoelectron spectroscopy (XPS) was used to analyze the chemical composition of Fe(III)/Cu(II)@silica.[20,21] The XPS survey spectra for the sample are shown in Fig. 6, while the high-

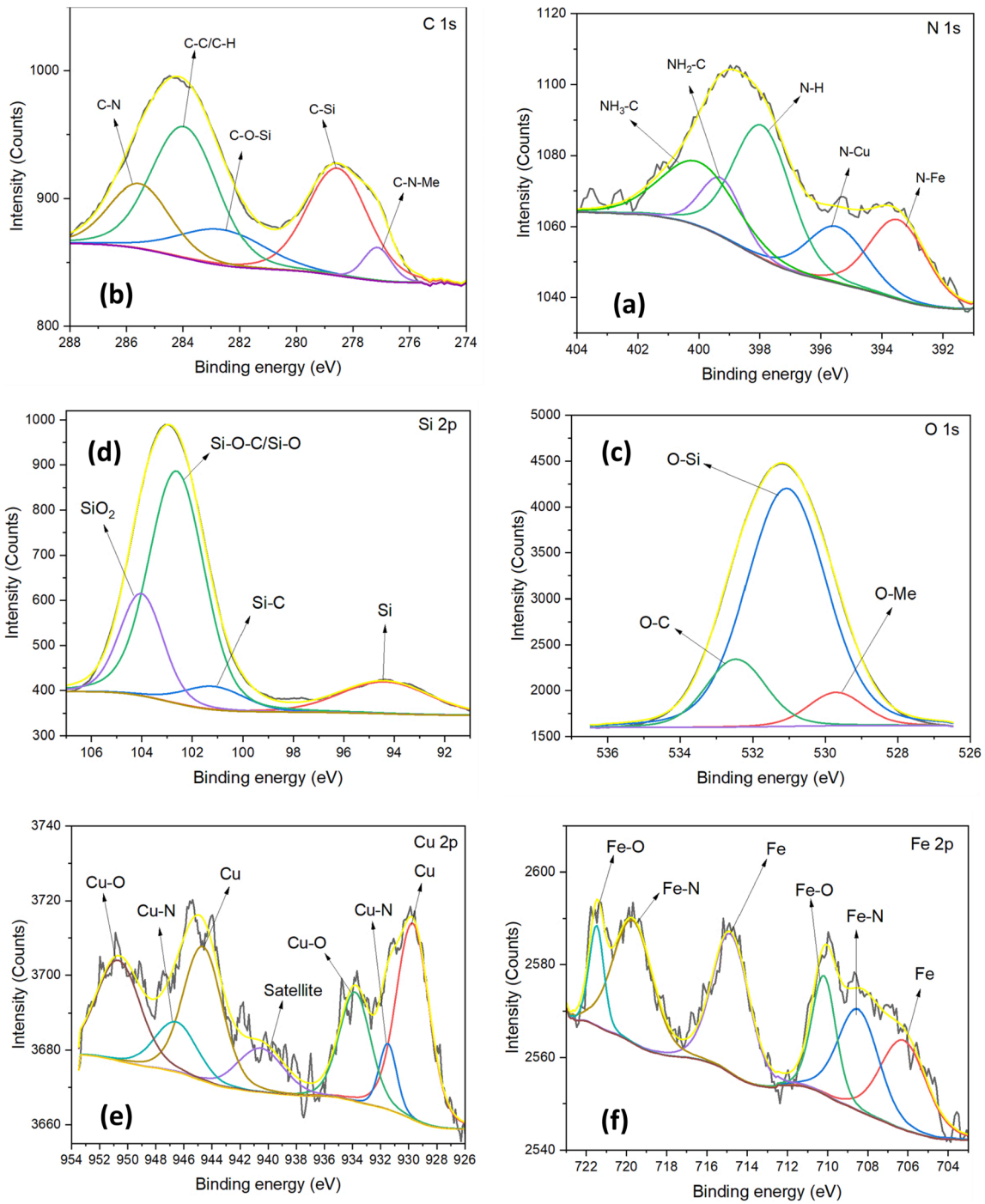

Fig. 7 Deconvolution of the high-resolution (a) N 1s, (b) C 1s, (c) O 1s, (d) Si 2p, (e) Cu 2p, and (f) Fe 2p spectra of the Fe(III)/Cu(II)@silica composite.

resolution de-convoluted spectra for C 1s, O 1s, N 1s, Si 2p, Fe 2p, and Cu 2p are presented in Fig. 7. The elemental composition of the sample includes carbon, oxygen, nitrogen, silicon, iron, and copper at 15.25 at%, 40.52 at%, 1.80 at%, 41.57 at%, 0.29 at%, and 0.57 at%, respectively. These results confirmed the successful synthesis of Fe(III)/Cu(II)@silica.[22]

The chemical states and bonding information of the elements are shown in Fig. 7(a); the N 1s spectrum reveals five distinct peaks, corresponding to N–Fe (394.47 eV), N–Cu (396.48 eV), N–H (398.93 eV), NH_2–C (399.26 eV), and NH_3–C (400.36 eV) within the Fe(III)/Cu(II)@silica chemical structure.[23,24] Fig. 7(b) presents the high-resolution C 1s spectrum, where the peak is deconvoluted into five components, namely, C–N–M (278.14 eV), C–Si (279.55 eV), C–O–Si (283.63 eV), C–C/C–H (284.80 eV), and C–N (286.54 eV), where "M" refers to the metal (Cu or Fe).[25,26] The O 1s spectrum displayed in Fig. 7(c) shows the presence of O-M (Fe and/or Cu), O–Si, and O–C bonds, as confirmed by peak deconvolution. In Fig. 7(d), the Si 2p spectrum reveals four peaks: one at 95.36 eV, consistent with non-metallic silicon, and the others at 102.14, 103.62, and 105.02 eV, representing Si–C, Si–O–C/Si–O, and O–Si–O bonds, respectively.[27] The high-resolution XPS spectra of Fe 2p and Cu 2p are shown in Fig. 7(e and f), which is divided into three doublet peaks of metallic elements, Fe/Cu–N bonds and Fe/Cu–O bonds, respectively. The presence of metallic iron and copper in the nanocomposite demonstrates the formation of the metallic nanoparticles. The doublet Fe 2p peaks at 709.48 eV (Fe $2p_{3/2}$) and 720.68 eV (Fe $2p_{1/2}$) correspond to the Fe metal bond of Fe–N, and the doublet Cu 2p peaks at 932.48 eV (Cu $2p_{3/2}$) and 947.56 eV (Cu $2p_{1/2}$) correspond to the Cu metal bond of Cu–N. The other doublet Fe 2p peaks that appeared at 711.18 eV and 722.49 eV are assigned to Fe $2p_{3/2}$ and Fe $2p_{1/2}$ of Fe–O, and the peaks at 934.81 eV and 951.66 eV are assigned to Cu $2p_{3/2}$ and Cu $2p_{1/2}$ of Cu–O, suggesting that a proportion of the metals are oxidized.[28] It was reported that for iron forming a bond with the NH_2-group, the Fe($2p_{3/2}$) binding energies are identified between 707.5 and 709.7 eV. For the Fe($2p_{1/2}$) binding energy of Fe–NH_2 bond, the values vary between 720 eV and 730 eV depending on the oxidation state and chemical environment around the binding elements.[29,30]

3.5 Thermogravimetric analysis

The TGA curve of the synthesized nanocomposite is given in Fig. S1. Accordingly, the first (25–150 °C) and second (150–430 °C) mass losses were about 13.66% and 2.17% due to the evaporation of water molecules adsorbed on the surface and the decomposition of the amine-based organic compounds, respectively.[31] The remaining ash at 750 °C (about 81% of the initial mass of the nanocomposite) contained copper-based substances, iron-based substances, and SiO_2 with high thermal stability, as well as thermally decomposed organic substances.

3.6 BET analysis

BET analysis was performed to evaluate the specific textural properties of the materials, with nitrogen adsorption used to assess the surface area and pore volume. The surface area was determined using the BET (Brunauer–Emmett–Teller) equation. The average pore radius was estimated from the BET surface area and total pore volume, assuming an open cylindrical pore model without pore networks. The BJH (Barrett–Joyner–Halenda) method was also employed.[32,33] Amine-modified silica (amine@silica) was used as a reference to compare with Fe(III)/Cu(II)@silica for investigating the impact of Fe(III) and Cu(II) on the surface characteristics. Fig. S2 displays the nitrogen adsorption–desorption isotherms for amine@silica and Fe(III)/Cu(II)@silica. The adsorption rate of an adsorbent is known to depend on its surface area and pore volume, with larger surface areas typically leading to higher adsorption rates.[34] As displayed in Fig. S2(a), both samples show a high adsorption rate at low P/P_o values, which gradually decreases as the relative pressure increases. The isotherms follow type I of the IUPAC classification, indicating microporous structures. The significant uptake at low relative pressures is attributed to adsorption in micropores. Additionally, the hysteresis loop of type H4 in both isotherms suggests monolayer–multilayer adsorption, followed by capillary condensation in narrow slit-like pores.[35] The BET surface area of amine@silica was found to be 500.54 $m^2\ g^{-1}$, whereas for Fe(III)/Cu(II)@silica, it was 446.07 $m^2\ g^{-1}$, indicating that amine@silica has a larger surface area. The total pore volume, based on the BET theory, was 0.279 $cm^3\ g^{-1}$ for amine@silica and 0.262 $cm^3\ g^{-1}$ for Fe(III)/Cu(II)@silica. In the *t*-plot diagrams, the slope represents the external surface area, as shown in Fig. S2(b). The external surface area was 27.69 mmol g^{-1} for amine@silica and 26.75 mmol g^{-1} for Fe(III)/Cu(II)@silica, suggesting that the presence of metal nanoparticles reduces the external surface area by blocking some of the micropores. From the *t*-plots, the micropore volume for amine@silica and Fe(III)/Cu(II)@silica was calculated as 17.64 $cm^3\ g^{-1}$ and 32.23 $cm^3\ g^{-1}$, respectively. The mesopore volume, obtained by subtracting the micropore volume from the total BET pore volume, was 17.36 $cm^3\ g^{-1}$ for amine@silica and 31.97 $cm^3\ g^{-1}$ for Fe(III)/Cu(II)@silica. As shown in Fig. S2(c), the pore width distribution for both samples was narrow, with most values under 10 nm. The BJH desorption cumulative surface area for pores ranging from 1.7 nm to 300 nm was 197.65 $cm^2\ g^{-1}$ for amine@silica and 295.61 $cm^2\ g^{-1}$ for Fe(III)/Cu(II)@silica. The average pore diameter, based on BJH desorption, was 2.96 nm for amine@silica and 2.73 nm for Fe(III)/Cu(II)@silica.

3.7 Electrochemical characterization

3.7.1. Electrocatalytic performance of different surfaces for the HER. Fig. 8 represents the evaluation of the HER characteristics over the synthesized materials in 0.5 M H_2SO_4 at a scan rate of 5 mV s^{-1}. The comparison of the electrocatalytic performances of the different surfaces shows the effect of the type of modifier used concerning hydrogen generation. Linear sweep voltammetry (LSV) plots of different electrode surfaces, namely GC, GC/CNT, GC/CNT-Fe(III)@silica, GC/CNT-Fe(II)/Cu(II)@silica and GC/CNT-Fe(III)/Cu(II)@silica in an acidic medium. The different surfaces are compared to the GC (bare)

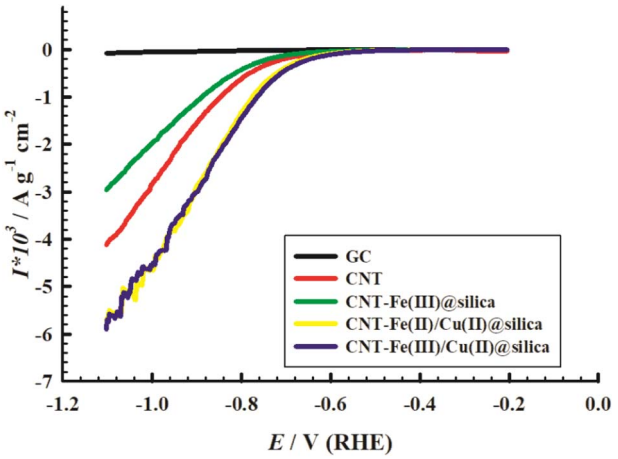

Fig. 8 Linear sweep voltammogram curves of different electrode surfaces in 0.5 M H_2SO_4 at a scan rate of 5 mV s^{-1}.

surface in relation to the HER. The order of the onset potentials for the HER as derived from the plots of Fig. 8 is: −0.704 V, −0.687 V, −0.634 V and −0.625 V *versus* RHE for the electrodes GC/CNT, GC/CNT-Fe(III)@silica, GC/CNT-Fe(II)/Cu(II)@silica and GC/CNT-Fe(III)/Cu(II)@silica, respectively. In order to drive a specific current of 100 A g^{-1} cm^{-2} the following overpotentials are required: −0.737 V, −0.706 V, −0.649 V and −0.631 V for the GC/CNT, GC/CNT-Fe(III)@silica, GC/CNT-Fe(II)/Cu(II)@silica and GC/CNT-Fe(III)/Cu(II)@silica electrodes, respectively. From the LSV data, the best electrocatalytic performance for the HER was exhibited by the GC/CNT-Fe(III)/Cu(II)@silica electrode. The GC/CNT-Fe(II)/Cu(II)@silica electrode showed close behaviour to that of the GC/CNT-Fe(III)/Cu(II)@silica electrode; we anticipated the relative stability of the second electrode with Fe(III) compared to Fe(II) in the first electrode. Therefore, the rest of the work will adapt the GC/CNT-Fe(III)/Cu(II)@silica electrode for this investigation. We determined the electroactive surface area of each electrode using a cyclic voltammetry (CV) technique in a $K_3[Fe(CN)_3]$-containing electrolyte (the CVs are provided in Fig. S3). The electroactive surface areas for GC, GC/CNT and GC/CNT-Fe(III)/Cu(II)@silica are 0.0615 cm^2, 0.177 cm^2, and 0.266 cm^2, respectively. The two-probe measurements using LCR bridge revealed the electrical conductivity of the samples as follows: SiO_2 (3.67×10^{-8} S cm^{-1}); CNTs (8.02×10^{-4} S cm^{-1}); and CNTs-Fe(III)/Cu(II)@silica (4.73×10^{-2} S cm^{-1}).

Previous publications indicated various values of overpotentials *versus* RHE to drive a current density of 10 mA cm^{-2}. A Cu–Fe mixture was prepared mechanically using a friction stirring process showing an overpotential of 67 mV to drive a current density of 10 mA cm^{-2}, using the same method of preparation for Fe and Cu; for Fe sheet and Cu sheet, the overpotentials are 169 mV, 297 mV, 406 mV and 418 mV, respectively.[36] A green method was reported for the preparation of cobalt ferrite ($CoFe_2O_4$), and the overpotential needed to drive a current density of 10 mA cm^{-2} was 440 mV.37 In another study, the following materials were chemically synthesized: Pt/C-20%, NiFe and $ZnFe_2O_4$; the corresponding values of the applied overpotentials to drive a current density of 10 mA cm^{-2} are as follows: 70 mV, 420 mV and 520 mV, correspondingly.[38] It is challenging to compare those figures with the values reported in this work since the mass of the catalyst was not reported. However, the GC/CNT-Fe(III)/Cu(II)@silica electrode, with a combined mass of CNT (0.5 mg) and Fe(III)/Cu(II)@silica (1.0 mg) in a stock solution of 1.0 mL in the electrolyte (only 10 μL are administered to the GC), displayed an impressive specific current of 1000 A g^{-1} cm^{-2} that needs an applied potential of −0.766 V *vs.* RHE.

The kinetics limiting the HER process was analyzed by the Tafel experiments using different electrodes. The Tafel analysis is discussed in terms of the Butler–Volmer equation and the derived equations thereafter:

$$j = j_o\left(e^{\frac{\alpha_A nF\eta}{RT}} - e^{\frac{-\alpha_C nF\eta}{RT}}\right) \quad (1)$$

where j_o is the exchange current density, α_A and α_C are the anodic and cathodic transfer coefficients, F is the faradaic constant (96 485.3 C mol^{-1}), R is the ideal gas constant (8.314 kJ·K^{-1}·mol^{-1}), T is the absolute temperature and η is the overpotential. The Tafel equation is derived as follows:

$$\eta = a + b\log(j) \quad (2)$$

where "a" is the intersection of the Tafel slope and "b" is the Tafel slope. The "a" and "b" parameters are simply expressed as follows:

$$a = -\frac{2.303RT}{\alpha F} \quad (3)$$

$$b = \frac{2.303RT}{\alpha F} \quad (4)$$

Fig. S4 displays the Tafel plots of different electrodes in 0.5 M H_2SO_4. The Tafel slopes derived from Fig. S4 in the high overpotential region ($|\eta|$ > 100 mV) are as follows: 462 mV dec^{-1}, 588 mV dec^{-1}, 316 mV dec^{-1} and 289 mV dec^{-1}, for the GC/CNT, GC/CNT-Fe(III)@silica, GC/CNT-Fe(II)/Cu(II)@silica and GC/CNT-Fe(III)/Cu(II)@silica electrodes, respectively. The Tafel slopes decreased, indicating the highest HER activity when using the GC/CNT-Fe(III)/Cu(II)@silica electrode. Different Tafel slope values have been reported previously in the literature for the HER at different electrodes and in various media. The Tafel slope obtained over $CoFe_2O_4$ is 98 mV dec^{-1} compared to those obtained at CuFe (144 mV dec^{-1}) and at $NiFe_2O_4$ (133 mV dec^{-1}).[37,38] A composite catalyst of platinum nanoparticles supported on a silica matrix (Pt/SiO_2) was synthesized. The electrocatalytic activity and stability of this catalyst were evaluated for the oxygen reduction reaction (ORR) using cyclic voltammetry and chronoamperometry.[39] The catalyst demonstrated a specific activity of 11.90 A g_{Pt}^{-1} normalized to a scan rate of 100 mV s^{-1}, which corresponds to a current density of 1.19 mA cm^{-2}. The stability was confirmed by the minimal decay in current over a 10-hour chronoamperometry test. In addition, the Tafel slope value for the HER is also structure dependent,[40] as it was reported for Pt with different

facets as 55 mV dec^{-1} and 150 mV dec^{-1} in a two-step kinetic for Pt(110). Some other electrocatalysts including "precious" metals were also reported for the HER and the corresponding Tafel slopes are 124 mV dec^{-1} for Ir/C, 127 mV dec^{-1} for Pd/C and 95 mV dec^{-1} for Rh/C measured within different overpotential regions in the fuel cell setup.[41] The relatively high Tafel slope values obtained in this study suggest that H_2O adsorption is energetically more favoured according to eqn (6) and (7) in the Volmer–Heyrovsky mechanism.[42] High Tafel slopes were obtained[43] over biogenic $CoFe_2O_4$ with a value of 283 mV dec^{-1} and an overpotential of 370 mV at a current density of 10 mA cm^{-2}.

$$H^+ + M \rightleftarrows MH_{ads} \text{ (Volmer step)} \quad (5)$$

$$MH_{ads} + H^+ + e^- \rightleftarrows H_2 + M \text{ (Heyrovsky step)} \quad (6)$$

$$2MH_{ads} \rightleftarrows H_2 \text{ (Tafel step)} \quad (7)$$

Eqn (5) represents the Volmer step where a hydrogen ion adsorbs over the active site of the catalyst M, and the second step shows the combination of the adsorbed hydrogen atom with another hydrogen ion (eqn (6); the Heyrovsky step); another possible route is the recombination of two adsorbed hydrogen atoms over the catalyst M to produce hydrogen (the Tafel step), as shown in eqn (7). From the value of the Tafel slope over the GC/CNT-Fe(III)/Cu(II)@silica electrode, the kinetics of the HER is controlled by the Volmer step as the limiting one in the mechanism. According to eqn (1)–(4), the exchange specific currents (J_o) and charge transfer coefficients (α) were determined, as depicted in Table 1. The high electrocatalytic efficiency of the GC/CNT-Fe(III)/Cu(II)@silica electrode towards the HER is represented by the highest value of the corresponding exchange specific current. It is worth to mention that the combined loaded amount of CNT and Fe(III)/Cu(II)@silica is limited to 1.5×10^{-5} g within a 10 μL administered to the substrate (GC) surface. The relatively high values of the transfer coefficient reflect the high irreversibility of the process.

Electrochemical impedance spectroscopy (EIS) provides useful information on the interfacial interaction on the electrode surface and on the electrocatalytic interactions of the modifying film. The Nyquist plots for different electrodes are displayed in Fig. S5 (with the electric circuit used in fitting the data in the inset), and the results of data fitting are given in Table S1. R_s represents the electrolyte resistance, R_p is the polarization resistance reflecting the ease of charge transfer at the interface, CPE is the capacitive component that shows the capacitance of the double layer built up along with the surface roughness, W is the "Warburg" diffusional resistance component, and χ^2 represents the goodness of the fitting of the multivariable components. The low value of R_p for GC/CNT-Fe(III)/Cu(II)@silica (X8) reflects the high catalytic activity of this surface compared to the other electrodes. The Warburg diffusional component shows the lowest resistance value for the same surface.

Table 1 Exchange current density and charge transfer coefficient calculated from the Tafel plots for different surfaces in 0.5 M H_2SO_4 at a scan rate of 1.0 mV s^{-1}

Surface	$J_o \times 10^3$/A g^{-1} cm^{-2}	α
GC	592.2	0.906
GC/CNT	612.9	0.909
GC/CNT-Fe(III)@silica	602.6	0.907
GC/CNT-Fe(II)/Cu(II)@silica	648.8	0.914
GC/CNT-Fe(III)/Cu(II)@silica	655.4	0.915

3.7.2. Effect of the amount of modifier loading and the type of carbon material on the performance of the electrode for the HER. Further optimization and study of the electrode performance towards hydrogen generation will be focused on Fe(III)/Cu(II)@silica. The electrocatalytic performance of the modified electrode depends to a great extent on different parameters. The prime effects are reasonable due to the type and amount of the modifier's ingredients. The effect of the loading amount of Fe(III)/Cu(II)@silica is considered, and the results are shown in Fig. 9. The modifiers are weighed and dissolved in 1.0 mL of dimethylformamide: x g Fe(III)/Cu(II)@silica (x = 0.5 mg, 1.0 mg, and 2.0 mg) and 0.5 mg CNT. A 10 μL

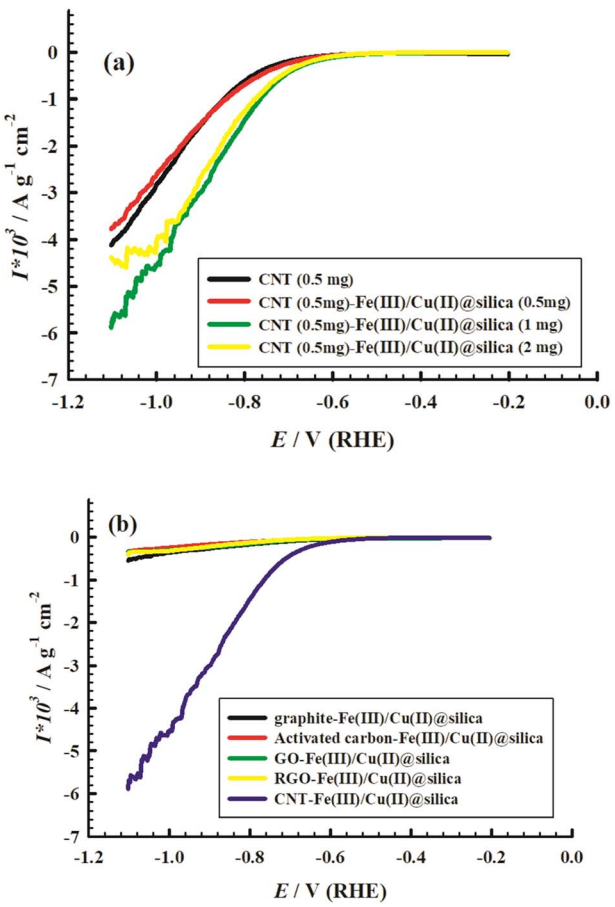

Fig. 9 (a) Linear sweep voltammograms of CNTs (0.5 mg) with different amounts of Fe(III)/Cu(II)@silica in 0.5 M H_2SO_4 at a scan rate of 5 mV s^{-1}. (b) Linear sweep voltammograms of different carbon materials with Fe(III)/Cu(II)@silica in 0.5 M H_2SO_4 at a scan rate of 5 mV s^{-1}.

aliquot is applied to the surface of GC substrate. The results indicate that as the amount of Fe(III)/Cu(II)@silica catalyst increases, the onset of the hydrogen evolution overpotential decreases. We compared the performance of the electrode towards the HER in the presence of different amounts of Fe(III)/Cu(II)@silica to the case of CNTs only. As can be deduced from the data presented in Fig. 9(a), the application of 0.5 mg of Fe(III)/Cu(II)@silica in the stock (1.0 mL) solution did not alter the onset of hydrogen evolution overpotential appreciably; the use of 1.0 mg or 2.0 mg of Fe(III)/Cu(II)@silica in the stock solution does not differ also in terms of the overpotential for the HER. The following studies were performed using a catalyst ink prepared with a concentration of 1.0 mg mL^{-1}. From this ink, 10 μL was drop-casted onto a glassy carbon (GC) electrode to achieve a catalyst loading of 0.1 mg cm^{-2} on the electrode's surface.

The second important factor influencing the performance of the modifier is the type of carbon-based material used to support Fe(III)/Cu(II)@silica. In this regard, the following carbon-based materials were used: graphite, activated carbon, graphene oxide (GO), reduced graphene oxide (RGO) and carbon nanotubes (CNT). The nominal amount in the stock of each carbon-based material is 0.5 mg and mixed with 1.0 mg of Fe(III)/Cu(II)@silica in 1.0 mL stock electrolyte; the amount administered to the GC after is 5.0×10^{-6} g. The employments of graphite, activated carbon, GO and RGO show less electrocatalytic property towards the HER. However, the use of CNTs as carbon-based material supports enhances the electrocatalytic properties of the surface. This is observed when calculating the onset overpotential value of the *I*/*V* linear sweep voltammograms of Fig. 9(b). Multiwalled CNTs were employed extensively in the modification of electrode surfaces for various electrochemical applications due to their exceptional physicochemical properties. CNT surface adsorption and penetration ability constitute an important property for their use as electrode modifiers. Moreover, the CNT has a good affinity for the formation of non-covalent structures with organic molecules. The relatively large surface area and conductivity of CNTs compared to other carbon-based materials allow its reception to the immobilization of various electrocatalysts. Moreover, the CNT surface can be modified using chemical or physical routes to form different functional groups on its surface. CNTs therefore prove to be the best choice to allow enhanced charge transfer between the electrolyte and the GC substrate, which results in noticeable performance towards the HER.[44–46]

3.7.3. Determination of the diffusion coefficient and reaction rate constant of the HER. The apparent diffusion coefficients (*D*) and the rate constants (*k*) of the HER using different electrodes were determined from the chronoamperometry experiments in 0.5 M H_2SO_4. The following equations were adapted for the determination of the above-mentioned parameters:[47,48]

$$I_p = nFAC_0D^{1/2}(\pi)^{-1/2}(t)^{-1/2} \quad (8)$$

$$I_C/I_L = \pi^{1/2}(k_c t)^{1/2} \quad (9)$$

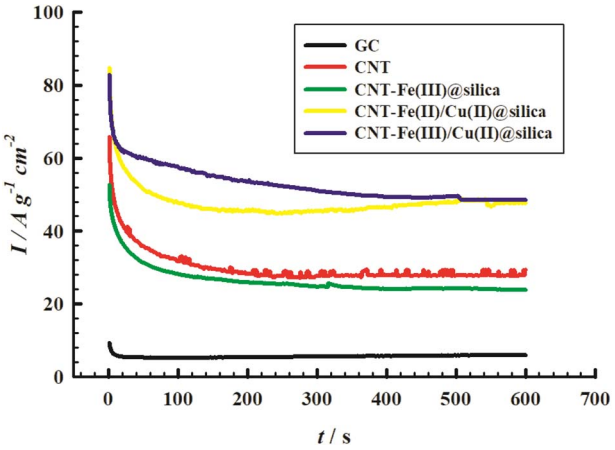

Fig. 10 Chronoamperograms over different electrode surfaces in 0.5 M H_2SO_4. The applied potential is −800 mV.

The parameters in eqn (8) and (9) are defined as follows: I_p is the specific oxidation current density of the catalytic process, *A* is the electrode area, C_0 is the concentration of the electrolyte, I_L is the current density value in the absence of electrolyte, and I_C is the current density value in the presence of electrolyte, *n* is the number of electrons exchanged during the catalytic process, *F* is Faraday's constant, *t* is the time, *D* is the apparent diffusion coefficient (cm^2 s^{-1}) and *k* is the catalytic rate constant (cm^3 mol^{-1} s^{-1}).

Fig. 10 shows the chronoamperogram curves over different electrode surfaces in 0.5 M H_2SO_4. The applied potential is −800 mV to ensure an appreciable rate of HER at different evaluated electrodes, as derived from the corresponding linear sweep voltammetry experiments (Fig. 8). Maximum "quasi-steady" specific currents are in the following order after running the experiment for 600 s for the different electrodes: GC < GC/CNT-Fe(III)@silica < GC/CNT < GC/CNT-Fe(II)/Cu(II)@silica ∼ GC/CNT-Fe(III)/Cu(II)@silica electrodes, respectively. It is expected that the GC/CNT-Fe(III)/Cu(II)@silica electrode shall drive the maximum current for the HER under an applied constant potential of −800 mV. As depicted in Fig. S6(a), a plot of the current densities I_p *versus* $t^{-1/2}$ shows linear relationships; using eqn (8), the values of the diffusion coefficients (*D*) can be calculated for the tested electrodes. The values of the apparent diffusion constants are given in Table 2. As expected, the order of increasing the values of *D* values is similar to those found for the "quasi-steady" specific currents

Table 2 Diffusion coefficient, *D*, and catalytic rate constant, *k*, for the HER in 0.5 M H_2SO_4 over different electrode surfaces. The applied potential is −800 mV

Surface	D/cm^2 s^{-1}	k/cm^3 mol^{-1} s^{-1}
GC	1.78×10^{-9}	—
CNT	6.06×10^{-8}	—
CNT-Fe(III)@silica	2.03×10^{-8}	7.55×10^{-3}
CNT-Fe(II)/Cu(II)@silica	7.58×10^{-8}	0.574
CNT-Fe(III)/Cu(II)@silica	7.55×10^{-8}	4.61

for the different electrodes as follows: GC < GC/CNT-Fe(III)@silica < GC/CNT < GC/CNT-Fe(II)/Cu(II)@silica ~ GC/CNT-Fe(III)/Cu(II)@silica. The main conclusion deduced from the results is that the presence of Cu(II) is critical for enhancing the efficiency of the HER process, as reflected from the diffusional component.

We compared the diffusion coefficient value for the HER at some surfaces. The D values for HER span between 10^{-5} cm^2 s^{-1} and 10^{-9} cm^2 s^{-1}, depending on several factors such as the type of electrolyte, temperature and electrode surface. For instance, Chen and his co-workers found that the D values obtained for the Mischmetal type (Mm) were of the order of 10^{-10} cm^2 s^{-1} for the $MmNi_5$ system alloys and 10^{-11} cm^2 s^{-1} for the Zr-based Laves phase alloys.[49] In another study, the diffusion coefficient using API 5L-grade X65 steel surface was found to have an average value of 4.12×10^{-9} m^2 s^{-1}, depending on the pH of the electrolyte and the applied overpotential.[50] It was also found that the shape and size of the electrode affect the value of the diffusion coefficient. For example, the D value for the HER at an ultra-micro electrode in 0.1 M KNO_3 was found to be 5.0×10^{-5} cm^2 s^{-1}[51] The value of the diffusion coefficient varied according to the crystalline nature of the electrode and the hydrogen pressure within the electrolyte. When performing the measurements using a rotating disc electrode on polycrystalline Pt in 0.1 M KOH with different hydrogen partial pressures (between 10 and 100 kPa H_2), the average value was found to be 3.4×10^{-5} cm^2 s^{-1}.

From eqn (9), the values of the rate constants for the HER can be estimated and Fig. S6(b) displays the relation between current ratios in 0.5 M H_2SO_4 *vs.* $t^{-1/2}$ at different electrodes with an applied constant potential of −800 mV. The calculated rate constants (k) are in the following order for the different electrodes: CNT-Fe(III)@silica < CNT-Fe(II)/Cu(II)@silica < CNT-Fe(III)/Cu(II)@silica. The synergistic effect from the combination of Fe(III) and Cu(II) is reflected in the high efficiency of the HER, which resulted in fast kinetic parameters. It is important to notice that most of the kinetic activation-controlled processes occur during the first few seconds from the application of the constant potential value as shown in the chronoamperograms of Fig. 10.

Evidence of the diffusional component on the charge transfer process for the HER is ascertained by changing the scan rate in the linear sweep voltammetry experiment. Fig. S7 shows the linear sweep voltammogram curves of CNT-Fe(III)/Cu(II)@silica in 0.5 M H_2SO_4 at different scan rate values (5–100 mV s^{-1}). The results showed that the onset potential for the HER shifts to lower values with the increase in scan rate. The value of the onset potential for the HER is −0.325 V *vs.* RHE for a scan rate of 100 mV s^{-1}. The performance of the present electrode modified with the catalyst CNT-Fe(III)/Cu(II)@silica is compared to some previously reported data for copper- and Fe-based catalysts with the figures of merit listed in Table S2.

3.7.4. Stability of the catalyst performance towards the HER. It is important to examine the stability of the used catalyst by monitoring current fluctuations and changes during an exhaustive experiment by applying a constant applied potential of −1000 mV *vs.* RHE during which the HER is continuously progressing over the electrode surface for an extended time. Fig. S8 shows the chronoamperometry experiment result for the CNT-Fe(III)/Cu(II)@silica electrode in 0.5 M H_2SO_4 under a relatively high overpotential to ensure a high rate of HER for one hour. As can be noticed, the current shows fluctuations due to the hydrogen evolution with adsorption/desorption of the gas on the electrode surface. The fluctuations during the one-hour experiment range in ±4.3% variation, indicating the stability of the current response within the test period. The experiment was repeated on the same electrode for a three-day interval, showing a standard deviation of 10.45%. The specific current change reflected that the electrode surface maintained its stability when stored in air. We also conducted extended exposure to exhaustive electrolysis for about 26 hours (Fig. S9) and found no substantial decay in current. The inductively coupled plasma measurement indicated relatively low dissolution of Fe from the surface of the electrode. We found the amount leaked as 0.36 μg after background correction, the % leakage to be 12.4 of the original amount loaded over the electrode surface.

3.7.5. Electrochemical performance of the catalyst towards the HER in different electrolytes. It is of prime importance to test the performance of the proposed catalyst, CNT-Fe(III)/Cu(II)@silica, in different supporting electrolytes. On the one hand, the electrode modified with the catalyst is tested in another acidic solution with different anions, $HClO_4$; the second electrolyte is a basic solution of KOH. The data are presented in Fig. S10–S14, Tables 3 and 4.

The analysis of the linear sweep voltammograms of Fig. S10 shows that the onset of the HER overpotential increases in the following order when using the CNT-Fe(III)/Cu(II)@silica catalyst in different electrolytes: KOH < H_2SO_4 < $HClO_4$. The onset overpotentials for the HER are as follows: −0.422 V, −0.631 V and −0.784 V when using the KOH, H_2SO_4, and $HClO_4$ electrolytes, respectively. While the overpotential needed to produce

Table 3 Exchange current density and charge transfer coefficient calculated from the Tafel plots for CNT-Fe(III)/Cu(II)@silica in 0.5 M of different electrolytes, namely, H_2SO_4, $HClO_4$ and KOH, at a scan rate of 1.0 mV s^{-1}

Electrolyte/0.5 M	$J_o \times 10^3$/A g^{-1} cm^{-2}	α
H_2SO_4	654.41	0.915
$HClO_4$	634.61	0.912
KOH	701.56	0.921

Table 4 Diffusion coefficient, D, and catalytic rate constant, k, of the HER for CNT-Fe(III)/Cu(II)@silica in 0.5 M of different electrolytes, namely, H_2SO_4, $HClO_4$ and KOH. The applied potential is −1000 mV

Electrolyte/0.5 M	D/cm^2 s^{-1}	k/cm^3 mol^{-1} s^{-1}
H_2SO_4	1.37×10^{-6}	15.79
$HClO_4$	1.00×10^{-7}	0.077
KOH	6.83×10^{-8}	1.49

hydrogen evolution in KOH is the lowest compared to those representing acid media, the slope of the *I–V* curve at higher potential domains is the lowest in KOH. Therefore, it is expected that the exchange current densities (J_o) are in the order of KOH > H_2SO_4 > $HClO_4$. The apparent diffusion coefficients (D) are however in the order of H_2SO_4 > $HClO_4$ > KOH, while the apparent rate constants (k) are in the order of H_2SO_4 > KOH > $HClO_4$. It is noticed that the slope of the *I–V* curve for the KOH electrolyte in Fig. S11 is lower than those for H_2SO_4 and $HClO_4$ at higher overpotential values. Although the rate constant is higher for KOH than for $HClO_4$ calculated at low overpotential values, the rate increases as the applied potential increases. The values of (J_o), (D) and (k) were calculated using eqn (8) and (9) from the data depicted in Fig. S12–S14. It was reported earlier that the kinetics and mechanism of the HER differ according to the type of acid used, and the nature of the surface and catalyst employed.[52] As shown in the present results, the proposed catalyst exhibits a lower overpotential for the HER than when tested in acidic media, and the diffusion coefficient and rate constant are smaller, indicating sluggish hydrogen evolution kinetics. Several previous reports have mentioned similar findings, and have been explained in terms of the low concentration of hydrogen ions in the solution, the barrier confronting the formation of the M–H bond, the type of catalyst employed, and the water association processes, and therefore, the "Volmer" step is rate-determining in alkaline media.[53–56] The following mechanism was suggested for the HER in an alkaline medium:[57]

$$H_2O + M + e^- \rightleftarrows MH_{ads} + OH^- \text{ (Volmer step)} \quad (10)$$

$$MH_{ads} + H_2O + e^- \rightleftarrows OH^- + H_2 \text{ (Heyrovsky step)} \quad (11)$$

$$2MH_{ads} \rightleftarrows H_2 \text{ (Tafel step)} \quad (12)$$

4. Conclusions

This work demonstrated a Fe(III)/Cu(II)@silica noble metal-free catalyst for an efficient HER that combines high performance and low cost. XPS confirmed the presence of Fe–Cu–N/O coordination bonds, which are critical for charge transfer. The high surface area (446.07 $m^2\ g^{-1}$) and porosity (0.262 $cm^3\ g^{-1}$, BET) of the hierarchical silica framework ensured rapid mass transport and accessible active sites. At low overpotentials (502 and 631 mV *vs.* RHE), the catalyst achieved ultrahigh current densities of 32.03 and 100 A $g^{-1}\ cm^{-2}$, outperforming in 0.5 M H_2SO_4. The Volmer step was found to be rate-limiting by the HER kinetics, which is regulated by a Tafel slope of 120 mV dec^{-1}, with a rapid HER rate constant of 4.61 $cm^3\ mol^{-1}\ s^{-1}$ (−800 mV *vs.* RHE). Carbon nanotubes (CNTs) support maximum conductivity and dispersion at ultra-loadings (1.5×10^{-5} g per 10 μL electrode). Comparative studies confirmed superior activity in H_2SO_4 due to optimal proton dynamics. The catalyst exhibited exceptional stability under industrial conditions (−1000 mV *vs.* RHE, 24 h), retaining >95% activity and exhibiting corrosion resistance and structural robustness. It is a good alternative to platinum-group catalysts due to its durability and low-cost Fe/Cu composition. By fusing hierarchical porosity with tailored coordination environments, this work advances the design of multifunctional heterostructures for sustainable hydrogen production. The Fe(III)/Cu(II)@silica system embodies innovation in materials and practical applications to address the challenges of efficiency and scale-up in renewable energy. By providing a scalable pathway to produce renewable hydrogen in line with global decarbonization goals, it aids in bridging the gap between high-performance catalysis and economic viability.

Conflicts of interest

The authors declare no conflict of interest.

Data availability

The data supporting the findings of this study, "Atomic-scale engineering of Fe–Cu nanoparticles on amine-functionalized silica: CNT-driven synergy for ultra-efficient hydrogen evolution", are available upon request.

Supplementary information is available. See DOI: **https://doi.org/10.1039/d5ra03709c**.

Acknowledgements

The authors would like to extend their gratitude to the King Abdulaziz City for Science and Technology (KACST) for their assistance in providing logistical and technical support.

References

1 F. Bao, E. Kemppainen, I. Dorbandt, R. Bors, F. Xi, R. Schlatmann, R. van de Krol and S. Calnan, *ChemElectroChem*, 2021, **8**, 195–208.
2 N. H. Khdary, M. A. Ghanem, M. E. Abdelsalam, D. N. Khdary and N. H. Alotaibi, *Int. J. Hydrogen Energy*, 2019, **44**(41), 22926–22935.
3 T. Im, J. W. Lee, S. C. Kim, S. Jun, J. S. Lee, M. S. Kim, J. K. Lee and S. Jeong, *J. Mater. Chem. A*, 2025, **13**, 9055–9063.
4 R. K. Joshi, S. Shukla, S. Saxena, G. H. Lee, V. Sahajwalla and S. Alwarappan, *AIP Adv.*, 2016, **6**, DOI: **10.1063/1.4941062**.
5 J. Zhang, T. Wang, P. Liu, S. Liu, R. Dong, X. Zhuang, M. Chen and X. Feng, *Energy Environ. Sci.*, 2016, **9**, 2789–2793.
6 W. J. Jiang, L. Gu, L. Li, Y. Zhang, X. Zhang, L. J. Zhang, J. Q. Wang, J. S. Hu, Z. Wei and L. J. Wan, *J. Am. Chem. Soc.*, 2016, **138**, 3570–3578.
7 R. Atchudan, T. N. J. Immanuel Edison, S. Perumal, R. Vinodh, N. Muthuchamy and Y. R. Lee, *Fuel*, 2020, **277**, 118235.
8 M. A. Qadeer, X. Zhang, M. A. Farid, M. Tanveer, Y. Yan, S. Du, Z. F. Huang, M. Tahir and J. J. Zou, *J. Power Sources*, 2024, **613**, 234856.

9 Z. Najaf, D. L. T. Nguyen, S. Y. Chae, O. S. Joo, A. U. H. A. Shah, D. V. N. Vo, V. H. Nguyen, Q. Van Le and G. Rahman, *Int. J. Hydrogen Energy*, 2021, **46**, 23334–23357.
10 M. Ďurovič, J. Hnát and K. Bouzek, *J. Power Sources*, 2021, **493**, 229708.
11 Y. Xu, Y. Liu, X. Zhang, K. Liu, R. Wang, Y. Yang, Z. Fang and J. Chen, *Int. J. Hydrogen Energy*, 2023, **48**, 757–765.
12 M. Liu, X. Yin, X. Guo, L. Hu, H. Yuan, G. Wang, F. Wang, L. Chen, L. Zhang and F. Yu, *Nano Mater. Sci.*, 2019, **1**, 131–136.
13 L. Memè, V. Notarstefano, F. Sampalmieri, G. Orilisi and V. Quinzi, *Materials*, 2021, **14**, 1–10.
14 J. Bandekar and S. Klima, *J. Mol. Struct.*, 1991, **263**, 45–57.
15 N. H. Khdary, W. S. Alkhuraiji, M. A. Ghanem and F. A. Alqureshah, *New J. Chem.*, 2017, **41**, 11556–11567.
16 N. H. Khdary and M. A. Ghanem, *J. Mater. Chem.*, 2012, **22**, 12032–12038.
17 Y. Liang, J. Ouyang, H. Wang, W. Wang, P. Chui and K. Sun, *Appl. Surf. Sci.*, 2012, **258**, 3689–3694.
18 N. Majoul, S. Aouida and B. Bessaïs, *Appl. Surf. Sci.*, 2015, **331**, 388–391.
19 N. H. Khdary, A. R. M. El-Gohary, A. Galal, A. M. Alhassan and S. D. Alzahrain, *RSC Adv.*, 2024, **14**, 25830–25843.
20 E. Gousseva, S. D. Midgley, J. M. Seymour, R. Seidel, R. Grau-Crespo and K. R. J. Lovelock, *J. Phys. Chem. B*, 2022, **126**, 10500–10509.
21 D. N. G. Krishna and J. Philip, *Appl. Surf. Sci. Adv.*, 2022, **12**, 100332.
22 K. Artyushkova, A. Serov, H. Doan, N. Danilovic, C. B. Capuano, T. Sakamoto, H. Kishi, S. Yamaguchi, S. Mukerjee and P. Atanassov, *J. Electron Spectrosc. Relat. Phenom.*, 2019, **231**, 127–139.
23 T. Yamashita and P. Hayes, *Appl. Surf. Sci.*, 2008, **254**, 2441–2449.
24 A. E. Hughes, C. D. Easton, T. R. Gengenbach, M. C. Biesinger and M. Laleh, *J. Vac. Sci. Technol., A*, 2024, **42**, 053205.
25 J. F. Moulder and J. Chastain, *Handbook of X-Ray Photoelectron Spectroscopy : a Reference Book of Standard Spectra for Identification and Interpretation of XPS Data*, Physical Electronics Division, Perkin-Elmer Corp., 1992.
26 M. C. Biesinger, *Surf. Interface Anal.*, 2017, **49**, 1325–1334.
27 D. Pleul, R. Frenzel, M. Eschner and F. Simon, *Anal. Bioanal. Chem.*, 2003, **375**, 1276–1281.
28 M. C. Biesinger, *Surf. Interface Anal.*, 2017, **49**, 1325–1334.
29 D. L. Peng, K. Sumiyama and M. Oku, *J. Mater. Sci.*, 1999, **34**, 4623–4628.
30 Y. Wang, L. L. Wang and C. Q. Sun, *Chem. Phys. Lett.*, 2009, **480**, 243–246.
31 S. Liu, Y. Chen, Y. Shi, H. Sun, Z. Zhou and T. Mu, *J. Mol. Liq.*, 2015, **206**, 95–102.
32 M. Saberi and P. Rouhi, *Fluid Phase Equilib.*, 2021, **534**, 112968.
33 F. Ambroz, T. J. Macdonald, V. Martis and I. P. Parkin, *Small*, 2018, **2**, 1800173.
34 J. Villarroel-Rocha, D. Barrera and K. Sapag, *Microporous Mesoporous Mater.*, 2014, **200**, 68–78.
35 J. Condon, *Surface Area and Porosity Determinations by Physisorption: Measurements and Theory*, 2006.
36 X. Z. Hu, C. Q. Cheng, X. Ji, Y. Feng, Z. Li, L. K. Meng, W. J. Kang, H. Liu, P. F. Yin, R. Zhang, L. Cui and X. W. Du, *Acta Mater.*, 2025, **284**, 120630.
37 R. P. Medang, R. Lontio Fomekong, E. A. Nforna, H. M. Tedjieukeng Kamta, C. N. Yonti, P. K. Tsobnang, J. N. Lambi and D. Bitondo, *Energy Adv.*, 2024, **3**, 1367–1374.
38 H. Belhadj, Y. Messaoudi, M. R. Khelladi and A. Azizi, *Int. J. Hydrogen Energy*, 2022, **47**, 20129–20137.
39 N. H. Khdary and M. A. Ghanem, *RSC Adv.*, 2014, **4**, 50114–50122.
40 N. M. Marković, B. N. Grgur and P. N. Ross, *J. Phys. Chem. B*, 1997, **101**, 5405–5413.
41 J. Durst, C. Simon, F. Hasché and H. A. Gasteiger, *J. Electrochem. Soc.*, 2015, **162**, F190–F203.
42 G. Q. Han, X. Li, Y. R. Liu, B. Dong, W. H. Hu, X. Shang, X. Zhao, Y. M. Chai, Y. Q. Liu and C. G. Liu, *RSC Adv.*, 2016, **6**, 52761–52771.
43 A. Panda, H. K. Cho and H. Kim, *Int. J. Mol. Sci.*, 2023, **24**, 9585.
44 Y. Lu, X. Chen, H. Lan, A. Nag, Y. Chen, J. Gao and S. Deng, *J. Alloys Compd.*, 2025, **1017**, 179106.
45 A. Leniart, B. Burnat, M. Brycht, M. M. Dzemidovich and S. Skrzypek, *Materials*, 2024, **17**, 841.
46 S. Karakaya and Y. Dilgin, *Monatsh. Chem.*, 2023, **154**, 729–739.
47 G. K. Gebremariam, A. Z. Jovanović and I. A. Pašti, *Hydrogen*, 2023, **4**, 776–806.
48 D. Grujicic and B. Pesic, *Electrochim. Acta*, 2002, **47**, 2901–2912.
49 J. Chen, S. X. Dou, D. H. Bradhurst and H. K. Liu, *Int. J. Hydrogen Energy*, 1998, **23**(3), 177–182.
50 L. Gritti, D. Coffetti, M. Cabrini and T. Pastore, *Int. J. Hydrogen Energy*, 2025, **112**, 347–353.
51 J. V. Macpherson and P. R. Unwin, *Anal. Chem.*, 1997, **69**, 2063–2069.
52 R. Punathil Meethal, R. Saibi and R. Srinivasan, *Int. J. Hydrogen Energy*, 2022, **47**, 14304–14318.
53 S. Bolar, S. Shit, J. S. Kumar, N. C. Murmu, R. S. Ganesh, H. Inokawa and T. Kuila, *Appl. Catal., B*, 2019, **254**, 432–442.
54 Z. Ma, R. Li, M. Wang, H. Meng, F. Zhang, X. Q. Bao, B. Tang and X. Wang, *Electrochim. Acta*, 2016, **219**, 194–203.
55 L. Jiang, S. J. Ji, H. G. Xue and N. T. Suen, *Int. J. Hydrogen Energy*, 2020, **45**, 17533–17539.
56 P. M. Pataniya, V. Patel, P. Sahatiya, D. J. Late and C. K. Sumesh, *Surf. Interfaces*, 2022, **34**, 102319.
57 S. Baiju, U. Masuda, S. Datta, K. Tarefder, J. Chaturvedi, S. Ramakrishna and L. N. Tripathi, *Int. J. Hydrogen Energy*, 2024, **51**, 779–808.